A bi-functional configuration for a metal-oxide film supercapacitor

By: Yiyang Liu, Zheng Zeng, Rama Krishna Sharma, Spero Gbewonyo, Kokougan Allado, Lifeng Zhang, and Jianjun Wei

Y. Liu, Z. Zeng, R. Sharma, S. Gbewonyo, K. Allado, L. Zhang, J. Wei, A bi-functional configuration for a metal-oxide film supercapacitor, *Journal of Power Sources*. **2019**, 409 (1), 1-5. https://doi.org/10.1016/j.jpowsour.2018.10.084.

Abstract:

Transition metal oxides can introduce high pseudocapacitance to an electric double layer capacitor for storing more electrical charges. Their role can be more than that since they possess high dielectric constant. Here, we propose a self-sustainable bi-functional configuration by eliminating traditional separator of a metal oxide film supercapacitor that is capable of providing good energy storage performance. We take advantage of super-aligned electrospun carbon nanofibers (SA-ECNFs) as an interconnected scaffold, coupling with electrochemical deposition of α-MnO_2 layers at different currents to introduce pseudocapacitance while providing dielectric layer functioning as a separator to assemble a state-of-the-art supercapacitor. The good electrochemical performance of galvanic charge-discharge specific capacitance at 141 F g^{-1} and energy density at 12.5 Wh kg^{-1} offers the promising applications in the energy storage field.

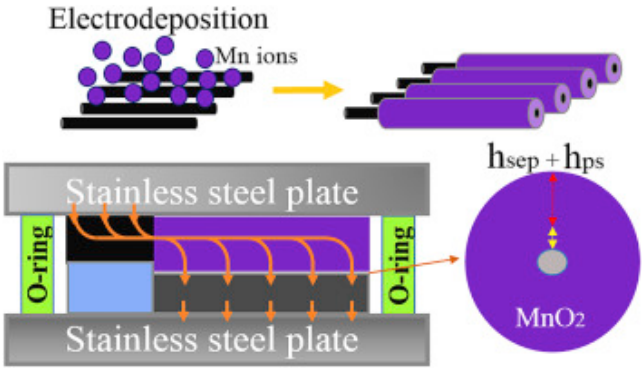

Keywords: Energy storage | Nano-architecture | Separator | Electrospun carbon nanofibers | Manganese dioxide

Article:

1. Introduction

Supercapacitors have been studied for decades and considered as one of the most promising energy storage systems [[1], [2], [3]]. Electric double layer capacitance (EDLC) capacitors utilize carbon or its derivatives as electrode followed with activation treatment to introduce pores and increase the specific surface area (SSA) [[4], [5], [6], [7], [8]]. Pseudocapacitance comes from the desolvated-adsorbed ions when active materials (usually transition metal oxides) are deposited onto EDLC electrodes, showing increased capacitance compared to EDLC [9,10]. Manganese dioxide (MnO_2) has demonstrated to be one of the most promising electrode materials for high pseudocapacitance [[11], [12], [13], [14], [15]], magneto property [16], electrocatalysis [17], eco-friendly, and low cost [18]. However, unstable MnO_2 loading inhibits the overall performance of a capacitor cell since the mass ratio of MnO_2/cell is very small. Researchers have tried to enhance the whole cell performance by increasing the mass concentration of MnO_2 in the cell [[19], [20], [21]]. Some studies offered solutions toward the commercially-viable level of MnO_2 mass loading [22], even though the accumulation of MnO_2 suffers from its low proton diffusion constant at about 10^{-13} cm^2 $(V\ s^{-1})^{-1}$ and low electrical conductivity ($\sim 10^{-5}$ S cm^{-1}) which can lower their galvanic charge-discharge efficiency [[23], [24], [25]].

A separator between two electrodes is a critical component in both lithium-ion batteries and supercapacitors. Its function is to provide an insulator between two electrodes while allowing free ions to flow through. They usually are polymeric membrane or non-woven fabric mat with thicknesses ranging from 25 μm to 200 μm [[26], [27], [28], [29]]. However the thicknesses of a typical supercapacitor electrode range from 100 nm to 120 μm [30,31], namely significant space (9.6%–50%) inside the cells was taken by the separator (Fig. S1), which may adversely affect their energy storage performance and product manufacturing. In principle, a separator provides low electric conductivity as insulator meanwhile offers channels for ions to transport. Manganese dioxide possesses internal pore structures which allow the permeation and rapid transport of ions to the nanoscopic MnO_2 phase [25]. The low electric conductivity [32] of MnO_2 meets the separator requirement in batteries and supercapacitors.

In our recent work, we reported a low-current controlled electrodeposition of metal oxides (e.g. MnO_2) on super-aligned electrospun carbon nanofibers (SA-ECNFs) (Fig. S2) [33]. The thickness of metal oxides can be tailored by the magnitude of current deposition and time while the aligned ECNFs provide advantages for the formation of uniform packed films [33]. Therefore, we propose to utilize the dielectric property of compact massive MnO_2 film loading to function as a separator, meanwhile to introduce pseudocapacitance energy storage to the SA-ECNF scaffold electrode. This is different from a previous report using graphene oxide film as separator in a supercapacitor in which the graphene oxide film demonstrates proton conductivity [34].

In this work, a new configuration of supercapacitor where the MnO_2 layer functions as both the pseudo-material and separator is presented. This novel design may save the space of a traditional separator and, more importantly, simplify the assembly procedure in the supercapacitor manufacturing. The SA-ECNFs are synthesized by a facile electrospinning setup with alignment (Fig. S3). A variety of uniform crystalline α-MnO_2 layers of thickness ranging 200 nm–2000 nm

onto SA-ECNFs as one of the electrodes in an asymmetrical supercapacitor cell are tested to examine the energy storage performance without using traditional separators.

2. Results and discussion

Fig. 1a–c schematically illustrate a new supercapacitor configuration of a non-separator design consisting of MnO_2/SA-ECNFs hybrid film as one electrode and a CNT paper as the other electrode for current collection. An insulator (3M vinyl electrical tape) was added to prevent the shortage between the end of the CNT paper electrode and the exposed SA-ECNFs end. The potion of SA-ENCFs coated with MnO_2 film and the CNT film form an asymmetrical cell without using traditional membrane separator for electrochemical and energy storage measurements. Note that the orange arrows display potential electron flows from current collector on the MnO_2 electrode side to the other side (Fig. 1b). The component preparation and testing device assembly are briefly described as follows. The SA-ECNF film was cut into 2×1 cm^2 pieces and half-immersed in the electrolyte for electrodeposition. The as-prepared MnO_2/SA-ECNFs hybrid film, CNT paper, and insulator were transferred into a glovebox then were assembled in a standard testing platform (Fig. 1c) [35]. The thicknesses of these films were carefully measured to ensure the good contact between the stainless steel plate as current collector and the supercapacitor electrodes (Fig. S4). A 6 M KOH electrolyte solution was sealed in the o-ring area in the cell (See SI for experimental details).

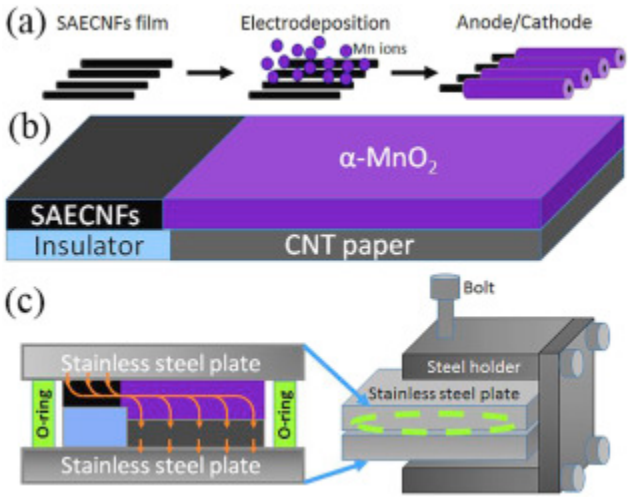

Fig. 1. Schematic processes of electrodeposition of MnO_2 (purple color film) on SA-ECNFs as a cathode (a), counter with CNT paper anode as an asymmetrical supercapacitor cell (b) and schematic illustration of a self-sustainable supercapacitor configuration consisting of anode, cathode, current collectors (stainless steel plate) and cell holder (c) without use of a membrane separator. (Orange arrows indicate the electron flows inside the cell). (For interpretation of the references to color in this figure legend, the reader is referred to the Web version of this article.)

Fig. 2a and b shows the low and high magnification scanning electron microscopy (SEM) images of the electrode materials. The as-prepared pure SA-ECNFs are aligned in an ordered structure. Our recent study indicates that the alignment of ECNFs can lead to a more uniform electrodeposition process for MnO_2 film formation. It is concluded that the growth of MnO_2 on SA-ECNFs follows a three-step mechanism including the final self-cessation based on the

electrodeposition time under a small electrodeposition current at μA level. Therefore, a variety of low currents (from 20 μA to 80 μA) were applied by an electrochemical workstation for electrodeposition at different time ranging from 0.5 h to 12 h to reach the self-cessation growth thus reaching the maximum film thickness (resultant details in Table S1) at each applied current. The composites' structure and morphology of the deposition were characterized by SEM (Fig. 2c–f, Fig. S5). The SEM images show a compact uniform MnO_2 films which wrap around the carbon fiber core (except the 20 μA deposition).

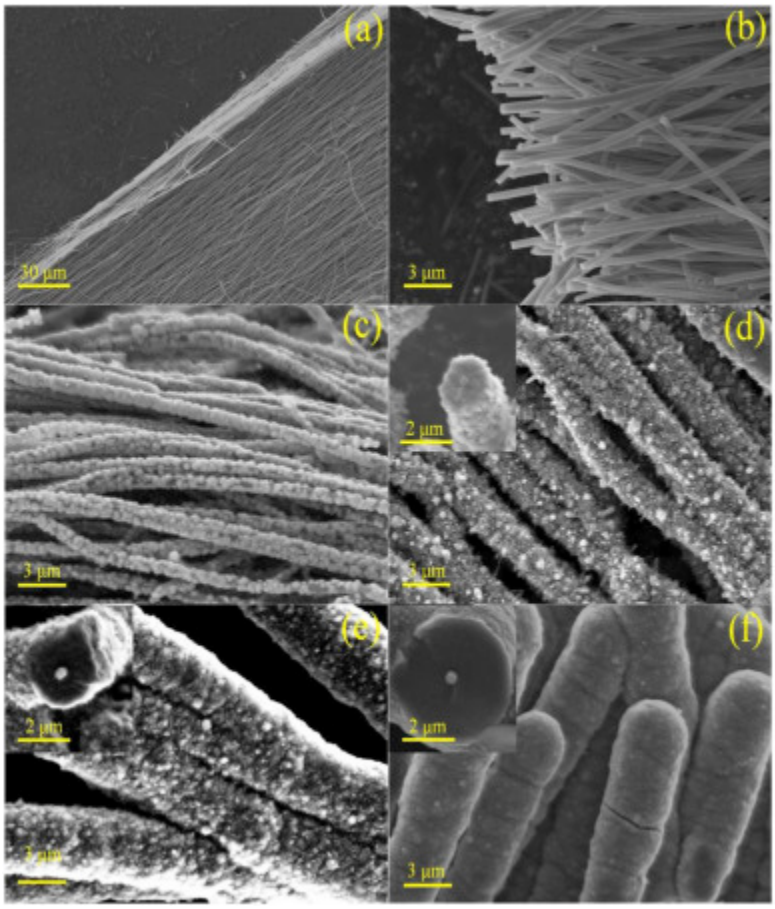

Fig. 2. SEM images of SA-ECNFs (a–b) and MnO_2 deposition on SA-ECNFs (c–f) at different deposition current and time until the film growth stops; c) 20 μA for 12 h, d) 40 μA for 4 h, e) 60 μA for 3 h, and f) 80 μA for 2.5 h, respectively. Insets are enlarged images to show the MnO_2 coating on SA-ECNFs films.

As discovered in our recent study [33], the MnO_2 film keeps growing as electrodeposition time increases until growth stops at a certain time point which depends on the magnitude of the deposition current. In this study, the SEM image shows the 20 μA electrodeposition could not achieve a uniform coating (Fig. 2c). When the electrodeposition current was higher than 20 μA, the current flow could keep depositing MnO_2 onto SA-ECNFs after all surface activation sites of the AS-ECNFs were occupied. Clusters merge with one another to form small balls around the SA-ECNFs then keep growing until the fibers are fully covered. Fig. 2d–f shows the fully covered structure of MnO_2/SA-ECNFs with single layer thicknesses ranging from 897 nm to 1971 nm under a deposition current ranging from 40 μA to 80 μA.

Fig S6 shows the thickness distribution of different deposition currents with the saturation of film growth. As an outstanding type of carbon fibers, SA-ECNFs have a horizontally aligned structure, which highly facilitates the electron flow through the fiber arrays for a uniform electrodeposition. The SA-ECNFs with diameters of 305 ± 53 nm (Fig. S7) were synthesized with a standard electrospinning method followed with stabilization and carbonization [36]. Then MnO_2 can be deposited onto the SA-ECNFs to form a thick layer, and its thickness (Fig. S6) and mass (Fig. S8) were measured. In general, the thickness of the MnO_2 film increases with the applied constant current until the formation of a compact film for a current of 40 μA or larger.

The as-prepared MnO_2/SA-ECNFs films were also characterized to study their chemical composition. The energy dispersive X-ray (EDX) analysis (Fig. S9) shows that the surface composition of the electrochemically deposited electrodes is composed of the elements C, O, and Mn. The atomic ratio of O and Mn is close to 2:1, which implies the formation of MnO_2. The chemical composition of the MnO_2/SA-ECNFs sample was also investigated by X-ray Photoelectron Spectroscopy (XPS). The high-resolution Mn 2p spectra for MnO_2/SA-ECNFs is presented in Fig. S10a. Two strong peaks at 642.5 and 654.0 eV can be clearly seen, corresponding to the Mn $2p_{3/2}$ and Mn $2p_{1/2}$ spin–orbit peaks of MnO_2, respectively [37,38]. The pronounced peak in the O 1s XPS spectrum (Fig. S10b) at 530.3 eV is assigned to Mn−O−Mn in the composite, and the peak at 531.2 eV can be assigned to Mn-OH formation [39,40]. To investigate the MnO_2 crystal structure, the as-prepared MnO_2/SA-ECNFs under different electrodeposition conditions were examined by X-ray diffraction (XRD). Compared to the results of SA-ECNFs only (Fig. S11a), the XRD patterns could be fully indexed to α-MnO_2 (JCPDS No. 44-0141) [41] as showed in Fig. S11b (show peaks at 2θ of 19°, 25.3°, 31.4°, 36.5°, 40.6°, 50.8°, 54.9°, 78.5° and 65.5° corresponding to the diffraction planes of 200, 220, 310, 211, 301, 411, 431, 002, and 332 of MnO_2 crystals, respectively). The intensity of the typical peaks become more distinct with higher electrodeposition current. Hence the MnO_2 film is dominant with α-MnO_2 crystal structure.

The resistance of MnO_2/SA-ECNFs electrodes with 40 μA (charge transfer resistance of about 330 Ohms), 60 μA (charge transfer resistance of about 511 Ohms) and 80 μA (charge transfer resistance of about 709 Ohms) electrodeposition was firstly deduced from the electrochemical impedance spectroscopy (EIS) Nyquist plots from 100 kHz to 0.01 Hz (Fig. 3a) and a Randles equivalent circuit model fitting (Fig. S12). These plots consist of a semicircle in the high-frequency region, which display an increase in charge transfer resistance of the MnO_2/SA-ECNFs electrodes with an increase in electrodeposition current [42,43].

To investigate the energy storage performance of the MnO_2/SA-ECNFs full cell, an asymmetric two-electrode supercapacitor system was assembled (Figs. 1 and S4) without the use of cellulose separator and a 6 M KOH aqueous is used as supporting electrolyte. Galvanic charge-discharge tests of different electrodes using the metal oxide-based bi-functional configuration without membrane separators were performed at current densities of 2.5 A g^{-1}, 5 A g^{-1} and 10 A g^{-1} in the asymmetric supercapacitor prototype. The charge-discharge curves are shown in Fig. 3b–d. Electrical shortcut happens during the charge-discharge testing of the 20 μA deposited electrode system due to the insufficient thickness and/or nonuniformity of MnO_2 film. Fig. 3e demonstrates the capacitance of the MnO_2/SA-ECNFs electrodes with 40 μA, 60 μA and 80 μA

deposition is 141 F g^{-1}, 91 F g^{-1}, 56 F g^{-1}, and Fig. 3f presents the energy density of 12.5 Wh kg^{-1}, 8.1 Wh kg^{-1}, and 5 Wh kg^{-1} with respect to the whole electrode mass, respectively.

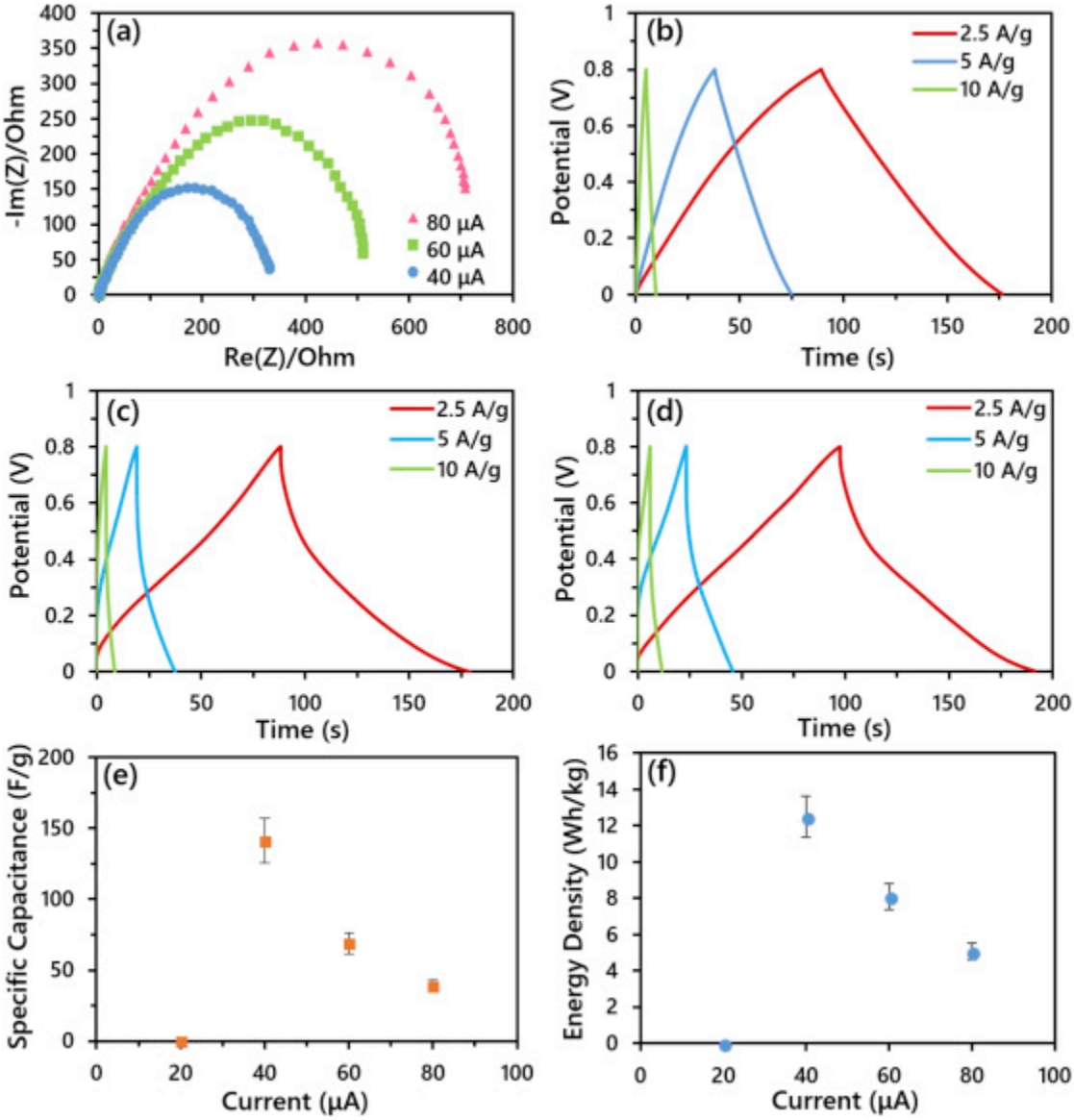

Fig. 3. Electrochemical characterization of the electrodes without separator: EIS from 100 kHz to 0.01 Hz (a); galvanic charge-discharge profiles at different current density (2.5 A g^{-1}, 5 A g^{-1} and 10 A g^{-1}) of MnO_2/SA-ECNFs electrodes with 40 µA (b) 60 µA (c) and 80 µA (d) electrodeposition; and their energy storage performance: specific capacitance (e) and energy density (f) with respect to the whole electrode mass (substrate + active material).

To examine the electrochemical behavior of the electrodes, cyclic voltammetry tests were conducted in a three-electrode setup where a gold electrode taped with MnO_2/SA- ECNFs served as the working electrode, platinum wire worked as the counter electrode, and Ag/AgCl as the reference electrode). Fig. S13 compares the cyclic voltammograms of the MnO_2/SA-ECNFs electrodes of scan rates at 5 mV s^{-1} to 50 mV s^{-1} under different deposition current and time. As it can be seen, deposition under higher current exhibits larger integrated curve area, indicating

the potentially higher absolute areal capacitance (80 μA > 60 μA > 40 μA > 20 μA). While considering the different mass loading and thickness of the MnO_2 layers, the MnO_2/SA- ECNFs under 20 μA deposition current has the highest specific capacitance from CV with respect to mass of the whole electrode. The capacitance calculated from CVs with 20 μA, 40 μA, 60 μA and 80 μA deposition is 652 F g^{-1}, 396 F g^{-1}, 142 F g^{-1} and 89 F g^{-1}, respectively. Note that the potential window was set to be 0.8 V based on the deviated CV shapes (comparing to the ideal rectangular shape) particularly at higher scan rates. Similar results can be found in our previous reports [33] and can be attributed to the obstructed tunneling of the electrolyte ions in the thick MnO_2 layers. The electric double layer capacitance of pure SA-ECNFs electrode has been examined under same conditions [16,33]. The capacitance is less than 2 F/g, about 1% of the total specific capacitance of MnO_2/SA-ECNFs electrode. Hence, the contribution of the SA-ECNFs in energy storage is insignificant and not considered in the following discussion.

The contribution of pseudo-capacitance depends on the reversible redox reactions between Mn(IV)/Mn(III) species and K^+ intercalation/de-intercalation at the MnO_2/electrolyte interfaces [[44], [45], [46]]. After a competing retention test at a current density of 2.5 A g^{-1} with and without the use of cellulose separator, the non-separator configuration shows an acceptable loss of energy density (Fig. S14) after 200 cycles. Fig. 3b presents a galvanic charge-discharge curve in a bulged triangle with 40 μA deposition current, suggesting pseudo-redox reaction in capacitance contribution. In contrast, Fig. 3c and d indicate concaved triangle curves with deposition current larger than 40 μA. The shape change of the galvanic charge-discharge curve may correlate to the significant increases of the resistance based on other reports of similar MnO_2 hybrid electrodes [16,[47], [48], [49]]. The 40 μA deposited electrode displays a good energy storage without using any separator in the testing setup, suggesting the feasibility of a self-sustainable bi-functional MnO_2 supercapacitor configuration based on uniformly coated metal oxide film-ECNFs electrodes.

A hypothesis of the bi-function of MnO_2 film at the electrode is proposed to describe energy storage mechanism. Assuming that the MnO_2 film contributes both the pseudocapacitance and the "separator" function, the assembled MnO_2/ENCFs electrode and its functions are depicted in Fig. 4a. The MnO_2 layer at the fiber surface is divided into two sublayers. The inter-layer near the carbon nanofiber surface is capable of electron penetration at a specific voltage during the charge/discharge process. The depth (d) is a function of applied voltage based on electron tunneling process in the dielectric material at contact and increases with a bigger applied voltage [50]. Within the inter-layer of MnO_2, the redox Mn(IV/III) reaction occurs during the charge/discharge process, thus contributes to the energy storage as the pseudocapacitance portion. The inter-layer thickness is defined as h_{ps} and equivalent or correlated to the electron "penetration" depth (d). If the deposited MnO_2 layer is thick enough, the outer-layer may act as a resistance barrier to avoid the direct shortage between two electrodes in the cell, thus functions as a "separator" (h_{sep}). In order to realize the self-sustainable bi-functional metal oxide configuration for a supercapacitor, the total thickness of deposited MnO_2 should be greater than the electron tunneling depth (d). In this work, 20 μA deposition for the saturated film is not sufficient to reach the tunneling depth.

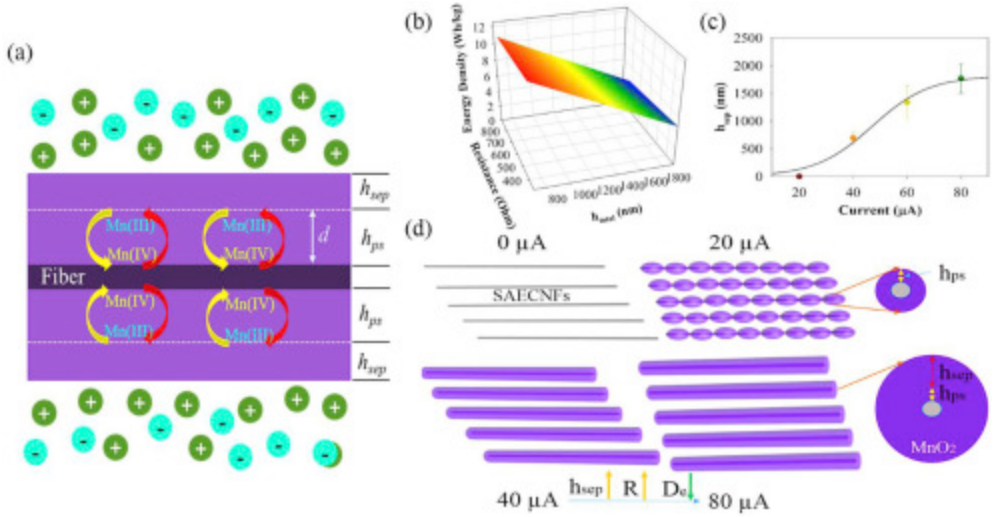

Fig. 4. (a) Proposed reaction mechanism of MnO_2 coated ECNF for energy storage with the bi-functional metal oxide configuration, (b) 3D plot of the correlation of the energy (D_e) with resistance and MnO_2 saturation thickness density from experiment. (c) The dependence of MnO_2 thickness as a separator role (h_{sep}) on the electrodeposition current fitted with an analytical model. (d) A schematic description of MnO_2 thickness as a pseudocapatance role (h_{ps}) and (h_{sep}).

We further analyzed the experimental results based on this proposed energy storage model. In this study, MnO_2 saturation thickness depends on the applied magnitude of electrodeposition current. The total thickness (h_{total}) can be divided into the inner-layer for the pseudocapacitance portion (h_{ps}) and the outer-layer for the "separator" function portion (h_{sep}). Note that h_{ps} contributes to the reversible redox reactions between Mn(IV)/Mn(III) species at the interlayer MnO_2/carbon interfaces while the resistance of h_{sep} is responsible to the separation function between two electrodes allowing free ions to flow and accumulate at the outer-layer MnO_2/electrolyte interface to avoid electrical shortage. Since the inner layer MnO_2 thickness is limited by the electron tunneling in the metal oxide, the higher h_{total} would lead to larger resistance (directly) and lower energy density (indirectly) (Fig. 4b). Herein, there is a tradeoff to the energy storage due to the resistance of the outer-layer MnO_2 functioning as "separator". To balance the pseudocapacitance and the separator role of MnO_2, an optimal electrodeposition current (I_{opt}) could be modeled. Using the energy density (D_e) results with respect to the deposition current (I), Fig. 4c shows the best fit of the h_{sep} versus electrodeposition current data (I) by an analytical equation (1):

$$h_{sep} = \frac{(h_{total} - d)_{\max}}{1 + e^{-\left(\frac{I - I_{opt}}{D_e}\right)}} \quad (1)$$

where the $(h_{total}\text{-}d)_{\max}$ represents the maximum outer-layer MnO_2 thickness allowing free ions to flow and accumulate, which is equivalent to the h_{sep} corresponding to different electrodeposition currents to their maximum thick MnO_2 deposition (Fig. 4d). The best fitting gives an I_{opt} of about 47 μA to reach the maximum energy density storage and the best h_{sep} can be obtained to be 983 nm, which is close to the result obtained from the 40 μA deposition-electrode in this work.

Galvanic charge-discharge tests of the same prototype using a cellulose separator indicate that MnO_2/SA-ECNFs electrodes obtained a higher specific capacitance and energy density (Fig. S15) from the 20 μA deposition-electrode with respect to the whole electrode mass. For the 40 μA or higher current deposition-electrodes, the bi-functional metal oxide configuration offers reasonable specific capacitance and energy density in a comparison to that of configuration with a membrane separator with respect to the electrode mass. Nevertheless, this new metal oxide-based bi-functional configuration can reduce the process of separator installation for supercapacitor production.

3. Conclusion

This work, for the first time, demonstrates a novel configuration of supercapacitor free of a traditional separator membrane by uniformly electrodepositing MnO_2 on aligned SA-ECNFs. The feasibility of MnO_2 layer functioning as both the pseudocapacitive material and separator in different thickness by changing the electrodeposition current was explored and confirmed. From the electrochemical performance, MnO_2/SA-ECNFs with 40 μA electrodeposition display a capacitance of 141 F g^{-1} and a specific energy density of 12.5 Wh kg^{-1}. This research presents a potential revolution of the metal oxide/carbonaceous nanomaterial-based pseudocapacitance energy storage by simply increasing the thickness of the metal oxide as replacement of a membrane separator, thus simplifying the manufacturing process.

Acknowledgement

This work is supported by NC state fund through Joint School of Nanoscience and Nanoengineering (JSNN), a member of Southeastern Nanotechnology Infrastructure Corridor (SENIC) and National Nanotechnology Coordinated Infrastructure (NNCI), which is supported by the National Science Foundation (ECCS-1542174).

Appendix A. Supplementary data

Supplementary data to this article can be found online at https://doi.org/10.1016/j.jpowsour.2018.10.084.

References

[1] A. Burke, J. Power Sources 91 (2000) 37–50.

[2] J.R. Miller, A.F. Burke, Electrochem. Soc. Interface 17 (2008) 53.

[3] Y. Wang, Z. Shi, Y. Huang, Y. Ma, C. Wang, M. Chen, Y. Chen, J. Phys. Chem. C 113 (2009) 13103–13107.

[4] L. Zhang, X. Yang, F. Zhang, G. Long, T. Zhang, K. Leng, Y. Zhang, Y. Huang, Y. Ma, M. Zhang, J. Am. Chem. Soc. 135 (2013) 5921–5929.

[5] Y. Wu, T. Zhang, F. Zhang, Y. Wang, Y. Ma, Y. Huang, Y. Liu, Y. Chen, Nano Energy 1 (2012) 820–827.

[6] Z.-F. Li, H. Zhang, Q. Liu, L. Sun, L. Stanciu, J. Xie, ACS Appl. Mater. Interfaces 5 (2013) 2685–2691.

[7] Y. Huang, J. Liang, Y. Chen, Small 8 (2012) 1805–1834.

[8] M. Zhi, S. Liu, Z. Hong, N. Wu, RSC Adv. 4 (2014) 43619–43623.

[9] Y. Liu, Z. Zeng, J. Wei, Front. Nanosci. Nanotech. 2 (2016) 78–85.

[10] M. Zhi, C. Xiang, J. Li, M. Li, N. Wu, Nanoscale 5 (2013) 72–88.

[11] G. Zhu, Z. He, J. Chen, J. Zhao, X. Feng, Y. Ma, Q. Fan, L. Wang, W. Huang, Nanoscale 6 (2014) 1079–1085.

[12] O. Ghodbane, J.-L. Pascal, B. Fraisse, F. Favier, ACS Appl. Mater. Interfaces 2 (2010) 3493–3505.

[13] O. Ghodbane, J.-L. Pascal, F. Favier, ACS Appl. Mater. Interfaces 1 (2009) 1130–1139.

[14] Z. Lei, F. Shi, L. Lu, ACS Appl. Mater. Interfaces 4 (2012) 1058–1064.

[15] H. Gao, F. Xiao, C.B. Ching, H. Duan, ACS Appl. Mater. Interfaces 4 (2012) 2801–2810.

[16] Z. Zeng, Y. Liu, W. Zhang, H. Chevva, J. Wei, J. Power Sources 358 (2017) 22–28.

[17] Z. Zeng, W. Zhang, Y. Liu, P. Lu, J. Wei, Electrochim. Acta 256 (2017) 232–240.

[18] J. Liu, J. Jiang, C. Cheng, H. Li, J. Zhang, H. Gong, H.J. Fan, Adv. Mater. 23 (2011) 2076–2081.

[19] L. Hu, W. Chen, X. Xie, N. Liu, Y. Yang, H. Wu, Y. Yao, M. Pasta, H.N. Alshareef, Y. Cui, ACS Nano 5 (2011) 8904–8913.

[20] Y. Hou, Y. Cheng, T. Hobson, J. Liu, Nano Lett. 10 (2010) 2727–2733.

[21] Y. Cheng, S. Lu, H. Zhang, C.V. Varanasi, J. Liu, Nano Lett. 12 (2012) 4206–4211.

[22] P. Lv, Y.Y. Feng, Y. Li, W. Feng, J. Power Sources 220 (2012) 160–168.

[23] Y. He, W. Chen, X. Li, Z. Zhang, J. Fu, C. Zhao, E. Xie, ACS Nano 7 (2012) 174–182.

[24] Z. Lei, J. Zhang, X. Zhao, J. Mater. Chem. 22 (2012) 153–160.

[25] D. Bélanger, L. Brousse, J.W. Long, Electrochem. Soc. Interface 17 (2008) 49.

[26] S.S. Zhang, J. Power Sources 164 (2007) 351–364.

[27] K.I. Ozoemena, S. Chen, Nanomaterials in Advanced Batteries and Supercapacitors, Springer, 2016.

[28] A. Subramania, N.K. Sundaram, G.V. Kumar, J. Power Sources 153 (2006) 177–182.

[29] G. Appetecchi, F. Croce, B. Scrosati, J. Power Sources 66 (1997) 77–82.

[30] X. Lang, A. Hirata, T. Fujita, M. Chen, Nat. Nanotechnol. 6 (2011) 232–236.

[31] J. Chmiola, C. Largeot, P.-L. Taberna, P. Simon, Y. Gogotsi, Science 328 (2010) 480–483.

[32] E. Preisler, J. Appl. Electrochem. 6 (1976) 311–320.

[33] Y. Liu, Z. Zeng, B. Bloom, D.H. Waldeck, J. Wei, Small 14 (2018) 1703237.

[34] Y.M. Shulga, S.A. Baskakov, V.A. Smirnov, N.Y. Shulga, K.G. Belay, G.L. Gutsev, J. Power Sources 245 (2014) 33–36.

[35] Y. Lu, F. Zhang, T. Zhang, K. Leng, L. Zhang, X. Yang, Y. Ma, Y. Huang, M. Zhang, Y. Chen, Carbon 63 (2013) 508–516.

[36] A. Aboagye, H. Elbohy, A.D. Kelkar, Q. Qiao, J. Zai, X. Qian, L. Zhang, Nano Energy 11 (2015) 550–556.

[37] S.W. Lee, J. Kim, S. Chen, P.T. Hammond, Y. Shao-Horn, ACS Nano 4 (2010) 3889–3896.

[38] Z. Wang, Z. Zhu, J. Qiu, S. Yang, J. Mater. Chem. C 2 (2014) 1331–1336.

[39] L. Yuan, X.-H. Lu, X. Xiao, T. Zhai, J. Dai, F. Zhang, B. Hu, X. Wang, L. Gong, J. Chen, C. Hu, Y. Tong, J. Zhou, Z.L. Wang, ACS Nano 6 (2012) 656–661.

[40] J.-G. Wang, Y. Yang, Z.-H. Huang, F. Kang, J. Mater. Chem. 22 (2012) 16943–16949.

[41] P. Yu, X. Zhang, D. Wang, L. Wang, Y. Ma, Cryst. Growth Des. 9 (2009) 528–533.

[42] C. Shang, S. Dong, S. Wang, D. Xiao, P. Han, X. Wang, L. Gu, G. Cui, ACS Nano 7 (2013) 5430–5436.

[43] J. Xu, S. Gai, F. He, N. Niu, P. Gao, Y. Chen, P. Yang, Dalton Trans. 43 (2014) 11667–11675.

[44] C. Liu, Z. Yu, D. Neff, A. Zhamu, B.Z. Jang, Nano Lett. 10 (2010) 4863–4868.

[45] Z. Fan, J. Yan, T. Wei, L. Zhi, G. Ning, T. Li, F. Wei, Adv. Funct. Mater. 21 (2011) 2366–2375.

[46] X. Dong, X. Wang, J. Wang, H. Song, X. Li, L. Wang, M.B. Chan-Park, C.M. Li, P. Chen, Carbon 50 (2012) 4865–4870.

[47] L. Yuan, X.-H. Lu, X. Xiao, T. Zhai, J. Dai, F. Zhang, B. Hu, X. Wang, L. Gong, J. Chen, ACS Nano 6 (2011) 656–661.

[48] J. Yang, L. Lian, H. Ruan, F. Xie, M. Wei, Electrochim. Acta 136 (2014) 189–194.

[49] L. Bao, J. Zang, X. Li, Nano Lett. 11 (2011) 1215–1220.

[50] K.C. Kao, 6 - charge Carrier injection from electrical contacts, Dielectric Phenomena in Solids, Academic Press, San Diego, 2004, pp. 327–380.